IMechE A: Journal of Power And Energy
XX(X):1–18

DOI: 10.1177/ToBeAssigned
www.sagepub.com/
SAGE

Analysis and optimisation of packed-bed thermal reservoirs for electricity storage applications

Alexander J White [1], Joshua D McTigue [1] and Christos N Markides [2]

Abstract

Several emerging electrical energy storage technologies make use of packed-bed reservoirs to store thermal energy for subsequent conversion back to electricity. The present paper describes analysis and optimisation of such reservoirs under transient and steady-state cyclic operation. The focus is on thermodynamic issues, but a simple costing model is also included in order to determine the influence of cost factors on the main design parameters. A major part of the paper is devoted to segmentation (or layering) of the packed beds which has previously been proposed as a means of simultaneously attaining high storage efficiency and full utilisation of the reservoirs. As illustrative examples, three different reservoirs are modelled, corresponding to the hot and cold thermal stores of a pumped thermal energy storage system, and a larger thermal store suitable for integration with adiabatic compressed air energy storage.

Keywords

Energy storage, packed beds, thermal reservoirs

Introduction

The increasing use of intermittent renewable generation technologies, such as wind and solar photovoltaics, and the inherent fluctuations in electricity demand, provide strong technical incentives for increasing the energy storage capacity of the grid. Currently, the UK has approximately 3 GW / 30 GW-h of storage, most of which is in the form pumped hydro schemes. In future scenarios with upwards of 20% of electricity generated by wind, it is estimated that many times this capacity will be required in order to meet the shortfalls caused by countrywide wind lulls, if reliance on fossil-fuel fired backup is to be avoided.[1]

Pumped hydro storage is both efficient and cost effective, but geographic constraints mean there is limited scope for its extension. Many new storage technologies are therefore emerging, an overview of which is given in Ref.[2] Several of these make use of thermal storage within packed beds. Examples include adiabatic compressed air energy storage (A-CAES) and pumped thermal energy storage (PTES), simplified layouts for which are shown in Fig. 1. In each case, compression work is converted (at least partly) to thermal energy which is then transferred from a hot gas to a bed of crushed rock or gravel. For the PTES system, part of the available energy is also stored in a cold thermal reservoir, typically at temperatures around $-150\ ^{\circ}\mathrm{C}$. Further descriptions and analyses of A-CAES and PTES systems can be found in Refs.[3–6]

For large-scale energy management applications (i.e., for time scales of hours or longer) cost and efficiency are two of the most important attributes of any storage technology. The overall 'round-trip' efficiency clearly depends on all the system components and the interactions between them. However, the present paper is concerned with the thermal reservoirs alone for which (in the context of electricity or 'work' storage) the efficiency may be defined as the ratio of the available energy (or exergy) returned during discharge to that absorbed during charge. This is affected to some extent by heat leakage to or from the surroundings, but the dominant factor is usually internal irreversibility, chiefly due to gas-particle heat transfer and frictional pressure drop. Segmentation (i.e., dividing the packed bed into horizontal layers), as proposed in Ref.[7], provides a means of mitigating the inherent conflict between these two sources of loss, but there is nonetheless a limit to the efficiency that can be achieved. Furthermore, the level of loss depends on the charge, storage and discharge history since it is governed to a large extent by the shape of the 'thermal fronts' (i.e., the temperature gradients) within the reservoir. These issues are addressed in this paper by numerical solution of the governing equations combined with simplified theoretical models of entropy generation rates. The main focus is on thermodynamic losses, but reducing these becomes increasingly expensive and it is thus impossible to undertake efficiency optimisation in isolation. A simple cost model is therefore included and the trade-off between efficiency and capital cost per unit of stored energy is examined.

Previous work

The literature relating to heat transfer within packed beds is vast, covering a wide range of applications, including chemical and drying processes, nuclear reactor

[1](Department of Engineering,) University of Cambridge, UK
[2] (Department of Chemical Engineering,) Imperial College, London, UK

Corresponding author:
Alexander J. White, Department of Engineering, University of Cambridge, Trumpington Street, Cambridge. CB2 1PZ, UK
Email: ajw36@cam.ac.uk

designs and thermal storage. The first analysis of packed-bed temperature transients dates back to 1926 and was undertaken by Anzelius[8]. This later developed into the well-known Schumann model which is essentially a one-dimensional, 'two-phase' model allowing for temperature differences between the gas and solid. Various numerical schemes based on the Schumann approach have since been developed and validated by measurements, as described in Ref.[9] Aside from these numerical models, an interesting closed-form solution has also been developed for cyclic operation of packed beds[10] but is not easily extendable to treat important practical effects such as the temperature dependence of the solid heat capacity.

Despite the numerous studies, there is relatively little work of direct relevance to electricity storage for which exergetic losses are of prime importance. A few studies have, however, examined some of these losses. For example, Bindra *et al*[11] consider the exergetic efficiency of a packed bed, accounting for gas-particle heat transfer loss and (particle) internal conductive effects, but do not consider pressure losses. Hänchen *et al*[12], have studied both thermal and fricitonal losses in a packed bed of rocks for concentrated solar power applications, concluding that efficiencies over 90% can be achieved, but their definition of efficiency is not consistent with a rigorous exergetic analysis. In the present paper all of the major loss components are considered and quantified formally as exergetic 'lost work' terms.

Notation

A	reservoir open area, m^2
b	specific availability, Jkg^{-1}
C_f	friction coefficient
c_{pg}	gas specific heat capacity, $\mathrm{Jkg}^{-1}\mathrm{K}^{-1}$
c_s	solid heat capacity, $\mathrm{Jkg}^{-1}\mathrm{K}^{-1}$
D	reservoir diameter, m
d_p	equivalent particle diameter, m
G	mass flow per unit area, $\mathrm{kgs}^{-1}\mathrm{m}^{-2}$
h	heat transfer coefficient, $\mathrm{Wm}^{-2}\mathrm{K}^{-1}$
h_g	gas specific enthalpy, Jkg^{-1}
k	thermal conductivity, $\mathrm{Wm}^{-1}\mathrm{K}^{-1}$
K	loss factors (see Appendix C)
ℓ	thermal length scale, m
$\dot{m}$	mass flow rate, kgs^{-1}
P	gas pressure, Nm^{-2}
$\dot{Q}$	heat flow rate, W
R	specific gas constant, $\mathrm{Jkg}^{-1}\mathrm{K}^{-1}$
$\dot{S}$	entropy generation rate, $\mathrm{JK}^{-1}\mathrm{s}^{-1}$
St	Stanton number
S_v	surface to volume ratio, m^{-1}
T	temperature, K
U_l	heat leakage coefficient, $\mathrm{Wm}^{-2}\mathrm{K}^{-1}$
U_w	thermal wave speed, ms^{-1}
W	work, lost work, J
z	axial distance, m
α	thermal diffusivity, $\mathrm{m}^2\mathrm{s}^{-1}$
ΔT	temperature difference, $T_c - T_d$ K
ϵ	packing void fraction
ρ	density, kgm^{-3}
μ_g	gas viscosity, $\mathrm{kgm}^{-1}\mathrm{s}^{-1}$
τ	time constants, s
θ	$(T - T_d)/\Delta T$

subscripts:

$c,\ d$	charge, discharge
$g,\ s,\ i$	gas, solid, insulation

Other symbols are defined in the text.

Method of analysis

A typical packed-bed reservoir comprises a solid packing material in the form of spheres, irregularly-shaped pebbles or gravel, surrounded by one or more layers of insulation and encased in a cylindrical containment vessel. The vessel may need to be pressurised, as is the case for both hot reservoirs shown in Fig. 1. The basic structure is illustrated in Fig. 2, together with the equivalent control volume used to derive the governing equations.

Governing equations

The equations governing heat exchange within packed beds are standard (see, for example, Ref.[9]) but are given here for completeness. The approach adopted is an extension of the Schumann model, the main assumptions being:

1. Solid and gas properties vary only in the $z-$direction. This is justified since particles are small compared to the bed diameter and because levels of insulation are sufficient to give only small radial variations and low levels of heat leakage (see Appendix B).
2. Gas-solid heat transfer, $\dot{Q}_x$, is limited by the thermal resistance at particle surfaces. This is justified on the basis of the small particles of interest and hence low Biot numbers.
3. Longitudinal conduction through the bed and heat leakage to the surroundings occur through and from the solid. This is merely a matter of convenience: the 'effective conductivity' (see below) models heat transfer through both the solid and gas.
4. Kinetic and potential energy terms for the gas flow are negligible.

With the above assumptions, the various heat transfer rates (see Fig. 2(b)) may be written as

$$\delta\dot{Q}_x = A(1-\epsilon)S_v h(T_g - T_s)\delta z \quad (1)$$

$$\delta\dot{Q}_l = \pi D U_l (T_s - T_0)\delta z \quad (2)$$

$$\delta\dot{Q}_c = -k_{\mathrm{eff}} A \frac{\partial^2 T_s}{\partial z^2}\delta z \quad (3)$$

where D and A are the packed bed diameter and cross-sectional area respectively, S_v is the particle surface-to-volume ratio, h is the gas-to-particle heat transfer coefficient and U_l is an overall heat transfer coefficient governing leakage through the insulation. Longitudinal heat transfer through the bed occurs by a variety of mechanisms (see, for example, Ref.[13]), but is modelled here by a single, constant conductivity, k_{eff}. Using the above expressions, the 1D conservation equations may be written as follows:-
mass:

$$\epsilon\frac{\partial \rho_g}{\partial t} = -\frac{\partial G}{\partial z} \quad (4)$$

momentum:

$$\epsilon\frac{\partial G}{\partial t} = -\frac{\partial}{\partial z}\left(\frac{G^2}{\rho_g}\right) - \epsilon(1-\epsilon)\tau_s S_v + \epsilon^2\left(\rho_g g - \frac{\partial p}{\partial z}\right) \quad (5)$$

gas energy:

$$\epsilon\left(\rho_g c_{pg}\frac{\partial T_g}{\partial t} - \frac{\partial p}{\partial t}\right) = h(1-\epsilon)S_v(T_s - T_g) - Gc_{pg}\frac{\partial T_g}{\partial z} \quad (6)$$

solid energy:

$$\rho_s(1-\epsilon)c_s\frac{\partial T_s}{\partial t} = k_{\text{eff}}\frac{\partial^2 T_s}{\partial z^2} + \frac{4U_l}{D}(T_0 - T_s) + h(1-\epsilon)S_v(T_g - T_s) \quad (7)$$

where $G = \dot{m}/A$ is the mass flow per unit area and τ_s is the effective shear stress on the particle surfaces. Note that ideal (not perfect) gas relations have been assumed, and that use has been made of the mass continuity equation in the derivation of Eq.(6).

Simplified model equations

Equations (4 – 7) are solved numerically using the method outlined in Appendix A. However, these equations can be considerably simplified with only minor approximations, leading to a clearer exposition of the physical processes. Firstly, the gas unsteady terms on the LHS of (4 – 6) and the momentum fluxes in Eq.(5) are all very small. This means that $G \simeq \text{const.}$ and the momentum equation thus simplifies to

$$\frac{\partial p'}{\partial z} = -\frac{G^2 S_v(1-\epsilon)C_f}{2\rho_g\epsilon^3} \quad (8)$$

where $p' = p - \rho_g g z$ and C_f is the friction coefficient. Similarly, the gas and solid energy equations reduce to

$$\frac{\partial T_g}{\partial z} = \frac{T_s - T_g}{\ell} \quad (9)$$

$$\frac{\partial T_s}{\partial t} = \frac{T_g - T_s}{\tau_x} + \alpha\frac{\partial^2 T_s}{\partial z^2} + \frac{T_0 - T_s}{\tau_l} \quad (10)$$

where ℓ and τ_x are length and time scales for gas-solid heat transfer:

$$\ell = \frac{1}{\text{St}(1-\epsilon)S_v} \quad \text{and} \quad \tau_x = \frac{\rho_s c_s}{Gc_{pg}S_v\text{St}}$$

St being the Stanton number, $h/(Gc_{pg})$. In Eq.(10) $\alpha = k_{\text{eff}}/(\rho_s c_s\{1-\epsilon\})$ is the effective thermal diffusivity of the bed, and $\tau_l = \rho_s c_s(1-\epsilon)D/(4U_l)$ is a time scale characterising heat leakage. It is worth noting that τ_l is typically tens or hundreds of hours, reflecting the relatively slow rate of heat leakage, whereas τ_x is usually just a few seconds.

These simplified equations have been used to guide the numerical integration scheme given in Appendix A, but they also provide physical insight into how the thermal fronts propagate and the nature of the loss-generating mechanisms. For example, combining Eq.(9) and Eq.(10) gives (see Ref.[14]):

$$\frac{\partial T_s}{\partial t} + U_w\frac{\partial T_s}{\partial z} = \frac{\ell}{\tau_x}\frac{\partial}{\partial z}\left(\ell\frac{\partial T_g}{\partial z}\right) + \alpha\frac{\partial^2 T_s}{\partial z^2} + \frac{T_0 - T_s}{\tau_l} \quad (11)$$

Since $T_g - T_s$ is usually very small, this equation shows that the progress of the thermal front may be viewed as wave convection at speed $U_w = Gc_{pg}/(\rho_s c_s\{1-\epsilon\})$ combined with two dissipative processes: one due to gas-particle heat transfer, the other due to axial conduction. The relative importance of these two sources of dissipation is determined by the ratio between the two effective diffusivities, $\alpha\tau_x/\ell^2 = k_{\text{eff}}/(Gc_{pg}\ell)$, which is also approximately the ratio between the conductive and thermal loss components, as shown in Appendix C.

Segmented reservoirs

Segmented packed-bed storage has previously been proposed as a means of retaining thermal stratification for solar applications[15]. In the current context it is used to allow greater control of the thermal front and to divert the gas flow such that it only passes through active regions of the reservoir containing the thermal front, thereby reducing pressure losses.

Figure 3 shows two possible segmented reservoir arrangements based on Refs.[7;16] In (a) the central baffle moves through the reservoir during charge tracking the thermal front, the intention being that the flow takes the path of least resistance so that, as shown, only layers B to D are active. In (b) each layer is individually gated allowing greater flexibility, as described further in the results and discussion. In practice, some flow will leak through the bypassed layers (as indicated by the dashed lines through layer E), depending on the flow resistance of the layers relative to the bypass channels.

Loss mechanisms

One of the main objectives of the present work is to establish the efficiency of the thermal storage process. Since the energy is to be recovered in the form of electrical (or possibly mechanical) work, this entails computing losses in available energy (or exergy) due to heat leakage and the various internal irreversibilities. These losses may be categorised as follows:

1. ***Thermal loss.*** For consistency with previous publications we use the term 'thermal loss' to refer to the gas-particle heat transfer irreversibility. The entropy generation rate associated with this process is

$$\dot{S}_t = \int\left(\frac{1}{T_s} - \frac{1}{T_g}\right)d\dot{Q}_x = \dot{m}c_{pg}\int_0^H \frac{(T_g - T_s)^2}{T_g T_s}\frac{dz}{\ell} \quad (12)$$

   the latter equality being obtained by substituting (1) and the expression for ℓ.

2. ***Pressure loss.*** The entropy generation rate due to pumping against friction is

$$\dot{S}_p = \dot{m}R\ln(p_1'/p_2') \quad (13)$$

where subscripts 1 and 2 refer to inlet and exit respectively. The pressure drop $(p'_1 - p'_2)$ is determined by integrating Eq.(8).

3. ***Conduction loss.*** Heat is conducted down the temperature gradient within the thermal front and this incurs a loss even when the reservoir is inactive (e.g., between charge and discharge). It therefore contributes to self-discharge of the storage system. The associated entropy generation rate may be shown to be:

$$\dot{S}_c = \int_0^H k_{\text{eff}} A \left(\frac{1}{T_s} \frac{\partial T_s}{\partial z} \right)^2 dz \qquad (14)$$

4. ***Heat leakage loss.*** Irrespective of the direction of heat flow, heat leakage to or from the environment reduces the stored available energy. As with axial conduction it occurs at all times and contributes to self-discharge. The rate of available energy loss is computed directly (rather than computing entropy changes) by multiplying the rate of heat loss (or gain) by the efficiency with which it could have been converted to work via a reversible heat engine. Thus,

$$\dot{W}_l = \int \left(1 - \frac{T_0}{T_s} \right) d\dot{Q}_l \qquad (15)$$

5. ***Exit loss.*** As a reservoir approaches full charge, hot (or cold) gas will emerge from its exit. The surplus available energy carried by this gas could in principle be recovered, but it is often impractical to do so. If all the surplus is wasted, the associated rate of work loss is

$$\dot{W}_x = \dot{m}_2 \{ b_g(T_{g2}, p_2) - b_g(T_d, p_2) \} \qquad (16)$$

where $b_g = h_g - T_0 s_g$ is the specific steady flow availability of the gas and T_d is the temperature of the reservoir in its fully discharged state. The exit loss cannot be calculated by considering the reservoir alone because the exit stream gets passed on to other components in the cycle. However, it is worth noting that, at least for cyclic operation, it is linked to (and is usually a small fraction of) the thermal loss[17].

The entropy generation rates in Eqs. (12-14) are converted to lost work terms by integrating with respect to time over the charge, discharge and (in the case of $\dot{S}_c$) intervening storage periods, and multiplying by T_0. The losses are then converted to loss coefficients by dividing by the net available energy input during charge.

Results and Discussion

Calculations have been undertaken for the hot and cold reservoirs (referred to as R1 and R2) of a 2 MW PTES system with a nominal 16 MWh of storage, using argon as the working fluid, and for a larger capacity reservoir (R3) of a 50 MW A-CAES system with a nominal 400 MWh of storage. (The nominal capacity is based on the difference between fully charged and fully discharged states and is not realised in practice.) Both simple (i.e., non-segmented) and segmented packed beds are considered for comparison, and the main parameters for each reservoir are given in Table 1.

Thermal front control

The shape of the thermal front within a packed bed depends on a number of factors, including particle size, history of operation and (for a segmented reservoir) the strategy for controlling the individual layers. Figure 4 (a) shows computed temperature profiles in the hot reservoir R1 during a single charge process, starting from a fully discharged state. Three cases are shown to illustrate the effect of front control using layers. Case (i) is a simple (non-segmented) reservoir, whereas cases (ii) and (iii) each have eight segments, labelled A–H. New segments at the leading edge of the thermal front are activated when the gas exit temperature from the previous layer exceeds 10% of the overall temperature rise ΔT (i.e., $\theta_{ge} \geq \theta_l$ in the figure). However in case (ii) trailing edge segments are deactivated when their exit temperature exceeds $\theta_h = 0.9$, whereas for case (iii) a maximum of two layers remain active at any time, similar to the situation shown in Fig. 3 (a). Note that profiles are shown at different values of t/t_N, where $t_N = H/\bar{U}_w$ is the nominal charge time.

For all three cases there is considerable growth of the thermal front as it progresses through the reservoir. For comparison, an 'ideal' front is shown at $t/t_N = 0.6$ (solid symbols in the figure), computed by pure convection of the profile, without dissipation, at the temperature-dependent wave speed U_w. This demonstrates that much of the growth is due to temperature dependence of the solid heat capacity and, since this is a reversible effect, a steeper, shorter thermal front will be recovered during discharge (see Ref.[14]). Nonetheless, growth of the front means that the reservoir cannot be fully charged without incurring a significant exit loss, as shown by the rising exit temperature beyond $t/t_N = 0.7$ in Fig. 4 (b).

Truncation of the nose and tail of the thermal front in the segmented cases (shown only at $t/t_N = 0.8$) clearly leads to steeper temperature profiles, but also generates a sawtooth wake in the deactivated segments. This decays with time, as indicated by the difference between the profiles in segments A and E of Fig. 4 (a). The sawtooth variations stem from the segment control strategy, and their magnitude depends on the values of θ_l and θ_h. (For example, if these are instead set to 0.01 and 0.99 respectively, the variations are barely discernable and the profile resembles that of a simple reservoir.) Detailed scrutiny of the profiles reveals that by $t/t_N \simeq 0.75$ case (iii) has attained a steady, repeatable state wherein the natural tendency of the thermal front to grow has been balanced by the sharpening of its leading and trailing edges due to the use of layers. The sawtooth wake in this case (which has not been shown to avoid overcrowding the figure) is however excessively pronounced and this particular method of control is probably impractical.

It might at first seem that the steeper fronts achieved by segmentation would enable the reservoirs to attain a higher state of charge, but this turns out not to be the case. This may be explained by considering the three cases described above at the same time t after the start of charge. In each case the same quantity of available energy will have entered the reservoir, but for the segmented reservoirs there will have been a small exit loss corresponding to the sawtooth variations of exit temperature shown in Fig. 4 (b). Furthermore, the steeper profiles imply that gas-solid heat

transfer occurs over a smaller interfacial area, leading to greater thermal irreversibility. The stored available energy is therefore almost always less in a segmented reservoir after a given period of charge *for a given particle size.* However, the advantage of segmentation is that smaller particles can be used without causing excessive pressure loss. The benefits of this are quantified in the section on optimum particle size.

Cyclic operation

An important application of storage is likely to be in levelling daily demand fluctuations. This requires the system to undergo 24-hour cycles, comprising consecutive charge, storage and discharge periods. This mode of operation is considered here but, for simplicity, the storage period has been omitted, and only 'symmetric' cycles have been computed, for which the charge and discharge periods are approximately equal. Figure 5 (a) shows computed temperature profiles within R1 for (i) an eight-layered reservoir with activation and deactivation thresholds $\theta_l = 0.1$ and $\theta_h = 0.9$, (ii) a simple reservoir with the same cycle period and (iii) a simple reservoir with a shorter cycle period. Starting from an initially discharged state, cases (i) and (ii) converged to regular, periodic operation after 3 or 4 cycles, whereas case (iii) required more than 20 cycles. Previous work (see Ref.[17]) has shown that the shape of the thermal front depends chiefly on the normalised charge period, $\Pi = t_c/t_n$. Thus in cases (i) and (ii) where $\Pi \approx 0.8$ the fronts remain quite steep and short, whereas in (iii), where $\Pi \approx 0.3$, they are much longer. The fronts grow during charge and shrink during discharge due to the temperature dependence of c_s, as discussed above. The longer front in case (iii) implies that heat transfer occurs over a larger gas-particle surface area leading to lower thermal loss, but this is at the expense of lower utilisation of the reservoir (only 30% of the nominal capacity is exploited in this case). This is one of the main factors causing a trade-off between cost and efficiency.

Exit temperatures and thermal losses for cases (i) and (ii) are shown as a function of time in Fig. 5 (b) for the first two cycles of operation. One of the practical advantages of segmented stores evident from this figure is that the exit temperature during discharge (and hence the returned power) remains closer to its maximum value. On the other hand, for a given particle size, thermal losses (lower plot) tend to be greater due to the transients associated with each activation and deactivation of the segments and due to the slightly steeper thermal fronts. Note that the transient peaks in loss observed during charge become notably smaller after the first cycle because the sawtooth wake left during the previous discharge process enables each new layer to be activated with only a small gas-solid temperature difference. By contrast, large temperature differences cannot be avoided at the trailing edge of the thermal front, creating loss spikes that are particularly pronounced during discharge.

By definition, cyclic operation requires the reservoir to periodically return to its initial state. The excess enthalpy flux due to the hot gas leaving during charge must therefore balance the deficit leaving during discharge. However, the net entropy efflux during each cycle must balance the entropy generated due to thermal irreversibility. This means that more hot gas (or at least gas with a higher average temperature) leaves during the charge process as Π is increased due to the steeper fronts and higher thermal losses. There is evidently a link between the thermal loss and the exit loss but the relationship is not straightforward. (Ultimately, the exit losses are best considered in the context of the complete storage system since they may well be recovered in susbsequent cycle components.)

Optimum particle sizes

As with most heat exchange processes, there is an inherent conflict between thermal and pressure losses within packed beds: small particles provide a large surface area thereby reducing thermal irreversibility but this is at the expense of a larger frictional pressure drop. One of the main advantages of segmented stores is that the pressure drop is confined to the active layers, thus allowing the use of smaller particles. Appendix C provides a simplified analysis of entropy generation rates due to the main sources of irreversibility for both simple and segmented stores, leading to algebraic expressions for the optimum particle size and the associated minimum loss. However, several approximations are involved and, in particular, it is difficult to accurately include the effects of variable c_s and the transients associated with segment activation and deactivation. Numerical predictions of the various loss components are thus presented here as a function of particle size and compared with results from the approximate analysis.

Figure 6 (a) shows computed loss components for the cold reservoir R2 operating cyclicly. The relatively low gas density in this reservoir leads to larger pressure losses and gives significant scope for optimisation. Results are shown for a simple reservoir and a reservoir with 64 segments, approximating the infinite-layered scenario described in Appendix C. In contrast to the segment control method described previously, the thresholds θ_l and θ_h have been set at 0.01 and 0.99 respectively, and the charge period held constant at $\Pi = 0.7$ by using larger thresholds for the first and last segments. This has the effect of providing temperature profiles that are very similar to the unlayered case, thus avoiding the loss spikes observed in Fig. 5 (b). With this strategy, segmentation can achieve a two to three-fold reduction in the pressure loss with only minor increases in thermal loss, as shown in Figure 6 (a). More aggressive truncation of the front (i.e., by increasing θ_l and reducing θ_h) would reduce pressure losses yet further but would be at the expense of greater thermal irreversibility. 1% thresholds provide a good compromise, though the optimum depends to a small extent on the number of layers.

Results of the approximate analysis given in Appendix C are also shown in Fig. 6 (a) as the square symbols. Optimum particle sizes are reasonably well predicted by this analysis, but the loss reduction from segmentation has been somewhat over-predicted. (The approximate method gives notably better results for reservoirs R1 and R3, as shown in Table 3). The main advantage of the approximate approach, however, is that it reveals the functional dependence of the minimum loss and optimum particle size on the main design parameters, thereby enabling the effects of scaling to be estimated.

Once reservoirs are in operation the particle size is of course fixed. However, as shown in Appendix C, the

optimum size depends on the dimensionless cycle period Π since greater utilisation of the reservoir implies steeper, shorter thermal fronts. It is therefore of interest to examine how a reservoir optimised for one value of Π behaves over a range of cycle periods. Figure 6 (b) shows results for R2 optimised at $\Pi = 0.7$. Note that utilisation in this plot is defined as the available energy returned per cycle normalised by the maximum value that would be obtained in the absence of losses and if the reservoir could be fully charged. The efficiency is defined as the available energy (exergy) returned during discharge as a fraction of that absorbed during charge. The figure demonstrates the effects of two different segment control strategies: in case A, Π is varied by adjusting the thresholds θ_l and θ_h for every segment, whereas in case B these thresholds are only varied for the top and bottom segments (elsewhere they are set at 1% and 99% of ΔT). Except at very low utilisation, the latter method maintains a better efficiency over the range of operation because loss spikes similar to those observed in Fig. 5 (b) are avoided. With this method, the benefits derived from segmented operation are clear and may be interpreted as either a modest increase in efficiency (2 to 2.5 percentage points) at high utilisation, or a substantial improvement in utilisation at fixed efficiency (e.g., an increase from 67 to 79% utilisation at an efficiency of 92%). However, the apparent improvement in utilisation will in practice be partially offset by the additional internal space required for bypass flows and by the cost associated with segment control mechanisms. In this regard it is worth noting that much of the benefit of an infinitely-layered store is achieved with just 8 layers.

Optimisation

It is difficult to undertake optimisation of reservoirs by systematic parameter variation due to the many different design variables and the complex interaction between them. A stochastic optimisation algorithm has therefore been applied to study the inherent conflict between cost and efficiency for the three reservoirs, R1 to R3. The routine chosen for this purpose is a non-dominated sorting genetic algorithm (NSGA-II), as described in Ref.[18] Like other stochastic methods, it is well suited to the current problem as it is able to traverse the entire design space without becoming trapped in local optima. Full thermo-economic analysis would require consideration of many different economic factors, including capital costs, operation and maintenance costs, electricity prices, subsidies and taxes. This is beyond the scope of the present study, which is limited instead to examining the influence of the main initial cost factors on the best choice of design parameters. A simple model that captures the main capital cost components is thus proposed and used to investigate the trade-off between storage efficiency and capital cost per kW-h of storage capacity.

Cost estimation

The main costs are for the containment vessel, the insulation and the storage material. Based on commercial data for pressure vessels and the experience of our industrial partners, the containment cost is assumed to be proportional to the product of pressure and internal volume. This gives a cost that is roughly proportional to, but significantly greater than, the raw steel cost, and thus includes labour costs for construction and welding etc. An additional component proportional to volume alone allows for unpressurised vessels. The total cost is thus estimated as,

$$C = k_s M_s + k_i V_i + k_c (P_0 + \Delta P) V \qquad (17)$$

where M_s is the mass of storage material, V_i is the volume of insulation, and ΔP and V are the vessel's internal gauge pressure and volume respectively. The parameters k_c and P_0 are set at $£200\ /\mathrm{m^3 bar}$ and 1 bar respectively. For the other components, data from the CES EduPack Materials Selector[19] suggest $k_s \sim £100\ /\mathrm{t}$ for magnetite and $k_i \sim £1000\ /\mathrm{m^3}$ for insulation with a modest conductivity of $0.05\ \mathrm{W/mK}$. These figures are of course subject to some uncertainty, but it is only their relative magnitudes that have a bearing on the optimised design parameters (i.e., on the engineering solutions).

As an example of the relative size of the different components, Fig. 7 shows costs as functions of temperature and storage capacity for pressurised reservoirs forming part of PTES (argon) and A-CAES (air) systems. [1] Containment cost dominates and is typically greater than 80% of the total. This means that the total cost per kW-h scales roughly as P/b_s, where the pressure P has been computed from isentropic relations and b_s is the available energy per unit mass of storage. b_s rises faster than P at low temperatures leading to a minimum that occurs at about $\sim 350\ ^\circ\mathrm{C}$ for air and $\sim 600\ ^\circ\mathrm{C}$ for argon. The rapid initial decrease in cost with reservoir size (Fig. 7 (b)) stems from the decreasing fraction of volume occupied by the insulation. Note that insulation thicknesses have been selected to keep heat leakage losses at 1% of internal energy per day, using the method described in Appendix B.

Cost and efficiency calculations

Table 2 shows lower and upper bounds of the design parameters varied during the optimisation process. For each reservoir optimisations have been undertaken with simple and segmented arrangements in order to show the improvements achieved by layering. Calculations for R3 (CAES) have been conducted with a fixed aspect ratio ($L/D = 3$), reflecting the importance of a small horizontal footprint for large-scale storage installations. In all cases, the mass of storage material and mass flow rate of working fluid are held constant, corresponding to fixed (nominal) storage capacity and fixed power respectively. Charge and discharge periods are allowed to vary (controlled by θ_c, θ_d, θ_l and θ_h), and the intervening storage periods are set such that the total cycle time is 24 hours. Insulation levels are chosen to give a nominal 0.5% (internal energy) loss per day and a maximum radial temperature variation of 10%, based on the method outlined in Appendix B.

The best designs for each reservoir are shown in Figure 8 (a) in the form of 'Pareto fronts'. These are the leading edges of the design space in that all other designs lie below or to the right of these fronts. It is notable that the margin between the simple and segmented results for R1 is quite small, suggesting that layering is of limited benefit for this case. This is due to the low value of K_p (see Appendix

C), reflecting the relative unimportance of pressure losses. Physically, this stems from the relatively high gas density, due to the high operating pressure. The somewhat larger margin for R3 (CAES) is partly due to the constraining of the aspect ratio: if L/D were allowed to vary, shorter and fatter reservoirs would be selected and the two fronts would be closer, but this would be at the expense of a larger footprint. Finally, the benefits of layering for R2 are clear, and in this case the highest efficiencies cannot be achieved by adjusting the aspect ratio alone. Of particular note is that high efficiency designs for R2 are significantly cheaper when layering is used [2].

Figure 8 (b) shows the distribution between the different sources of loss for the most efficient designs of R1 and R2 (points B and D in Fig. 8 (a)). Compared with the results presented in the cyclic operation section, there are additional losses due to heat leakage and the storage period (leakage plus conduction) which together constitute 30 to 40% of the overall loss. The conductive loss is more significant in these optimised designs as a consequence of the lower aspect ratios (0.85 for point B and 0.50 for D) which reduce G and thereby increase $\dot{S}_c/\dot{S}_t$ through Eq.(24). Leakage losses can of course be reduced by additional insulation, but conductive losses are tied to the steepness of the thermal fronts.

Figure 9 is a so-called parallax plot which compares values of the design parameters for optimal solutions. To avoid over-crowding, only four designs have been plotted (points A through D, corresponding to low cost and high efficiency extremes), but parallax plots for the full Pareto front reveal useful information on the best designs. For example, all solutions converge to values of θ_h close to 99%, whereas there is significant spread in the values of θ_l. This can be traced to the importance of reducing gas-solid temperature differences at the trailing edge of the front, as described in the cyclic operation section above. It is also possible to deduce that θ_c and θ_d (the dimensionless exit temperatures) are the main parameters controlling the trade-off between cost and efficiency: high values of θ_c combined with low values of θ_d yield long cycle periods and hence high reservoir utilisation which in turn give a low cost per unit of energy stored, but the steeper thermal fronts (see Fig. 5) result in higher losses.

Impact on overall efficiency

It is important to appreciate that the efficiencies given in Figure 8 (a) apply only to the thermal reservoirs. The overall round-trip efficiency of the complete energy storage system will of course be affected by losses in other components such as compressors, expanders, heat exchangers, motors and generators. Examples of system calculations and loss distributions between the different components for a PTES plant are given in Ref.[6] where it is seen that there is a rather complex interation between the different sources of loss. Nonetheless, it is possible to estimate the impact of reservoir losses on overall round-trip efficiency by simply weighting these losses by the fraction of exergy stored in each reservoir. For example, for a PTES system based on R1 and R2 (pressure ratio 10:1 and near-ambient exit temperatures during charge), roughly 70% of the exergy is stored in R1 and 30% in R2. Based on Figure 8 (a), individual efficiencies for R1 and R2 might be 98% and 94% respectively, so their aggregate efficiency is $0.7 \times 98 + 0.3 \times 94 = 96.8\%$, corresponding to 3.2% loss. A cycle calculation for this PTES system with 95% polytropic efficiency assumed for compressors and expanders (and no other losses) yields a round-trip effciency of 81.2%, whereas if reservoir losses are included this drops to 78.1%, roughly in line with the simple estimate above. (Note that this does not include electrical or mechanical losses.) Similar estimates may be undertaken for CAES systems, but account must be taken of the partition of stored exergy between packed beds, other types of thermal store and the compressed-air cavern (or equivalent).

Conclusions

The behaviour of packed-bed thermal reservoirs has been analysed using a numerical approach combined with simplified models of entropy generation rates. The main focus has been on determining thermodynamic losses and hence establishing the exergetic storage efficiency. The maximum value of this efficiency is determined chiefly by the balance between thermal, conductive and pressure losses, though heat leakage and exit losses also play some role. The simplified models allow the relative importance of these losses to be estimated via the coefficients K_t, and K_p and the conductive length scale ℓ_c, each of which is readily determined from reservoir design and operation parameters.

The use of segmented reservoirs is shown to reduce the minimum loss that can be achieved (i.e., with the optimum particle size), typically by between 25 and 50%. In the (hypothetical) case of a storage material whose heat capacity, c_s, is constant, the simplified model shows that this minimum loss is almost independent of the cycle time, and hence of reservoir utilisation. In practice, however, the temperature dependence of c_s causes reversible growth of the thermal fronts which limits the level of charge. Segmentation may also be used to provide a more constant power output during discharge, though this will usually be at the expense of some efficiency penalty.

As an alternative to segmentation, the minimum loss can also be reduced by adjusting the aspect ratio H/D of the reservoir. The approximate analysis suggests that the minimum loss scales as the mass flow rate per unit area, G, which in turn scales as $(H/D)^{2/3}$ for fixed power and storage capacity. However, altering the aspect ratio affects the required volume of insulation and therefore has implications for cost. A combined cost and efficiency optimisation suggests that segmentation of the packed beds may be particularly beneficial for the cold reservoirs of a PTES system, or for large CAES reservoirs that have a constrained footprint.

Acknowledgements

The authors gratefully acknowledge James MacNaghten, Jonathan Howes and Geoff Hunt of Isentropic Ltd. for many useful discussions and for partial funding of JDM.

Declaration of conflicting interests

AJW has previously undertaken consultancy work for Isentropic Ltd.

Funding

The work was undertaken as part of EPSRC project EP/J006246/1 on PTES. JDM was supported by an EPSRC studentship, with a small additional bursary from Isentropic Ltd.

Notes

1. The pressure vessels are assumed cylindrical with elliptical ends each of which has a volume half that of a hemisphere. This penalises low aspect ratio vessels, but $H/D = 1$ for all cases in Fig. 7.
2. The additional internal volume required for bypass flows and inter-layer gaps is included in the analysis by limiting the associated pressure losses to 10% of the overall pressure loss, but the extra costs of bypass valving, sensing and control systems needed for layering are not.

References

1. Mackay DJC. *Sustainable Energy without the Hot Air*. UIT Cambridge Ltd., 2009.
2. Luo X, Wang J, Dooner M et al. Overview of current development in electrical energy storage technologies and the application potential in power system operation. *Applied Energy* 2015; 137: 511 – 536.
3. Jakiel C, Zunft S and Nowi A. Adiabatic compressed air energy storage plants for efficient peak load power supply from wind energy: the european project aa-caes. *International Journal of Energy Technology and Policy* 2007; 5(3): 296–306.
4. Howes J. Concept and development of a pumped heat electricity storage device. *Proceedings of the IEEE* 2012; 100(2): 493–503.
5. White A, Parks G and Markides CN. Thermodynamic analysis of pumped thermal electricity storage. *Applied Thermal Engineering* 2013; 53(2): 291 – 298. Includes Special Issue: PRO-TEM Special Issue.
6. McTigue JD, White AJ and Markides CN. Parametric studies and optimisation of pumped thermal electricity storage. *Applied Energy* 2015; 137: 800 – 811.
7. Howes J, Hunt R and Macnaghten J. Improved heat storage apparatus, 2012. WO Patent App. PCT/GB2011/051,595.
8. Anzelius A. Heating by means of percolating media. *J of Mechanical Design* 1926; 6: 291–294. DOI: 10.1002/zamm.19260060404.
9. Schmidt FW and Willmott AJ. *Thermal Energy Storage and Regeneration*. Hemisphere Press, 1981.
10. Ni F and Caram HS. Analysis of pumped heat electricity storage process using exponential matrix solutions. *Applied Thermal Engineering* 2015; 84: 34 – 44.
11. Bindra H, Bueno P, Morris JF et al. Thermal analysis and exergy evaluation of packed bed thermal storage systems. *Applied Thermal Engineering* 2013; 52(2): 255–263.
12. Hnchen M, Brckner S and Steinfeld A. High-temperature thermal storage using a packed bed of rocks Heat transfer analysis and experimental validation. *Applied Thermal Engineering* 2011; 31(10): 1798–1806.
13. van Antwerpen W, du Toit C and Rousseau P. A review of correlations to model the packing structure and effective thermal conductivity in packed beds of mono-sized spherical particles. *Nuclear Engineering and Design* 2010; 240(7): 1803 – 1818.
14. White A, McTigue J and Markides C. Wave propagation and thermodynamic losses in packed-bed thermal reservoirs for energy storage. *Applied Energy* 2014; 130: 648–657.
15. Crandall D and Thacher E. Segmented thermal storage. *Solar Energy* 2004; 77(4): 435 – 440. The American Solar Energy Society's Solar 2003 Special Issue.
16. Howes J, MacNaghten J, Hunt R et al. Improved thermal energy storage apparatus, 2013. WO 2013/160650.
17. White A. Loss analysis of thermal reservoirs for electrical energy storage schemes. *Applied Energy* 2011; 88(11): 4150–4159. DOI:10.1016/j.apenergy.2011.04.030.
18. Deb K, Pratap A, Agarwal S et al. A fast and elitist multiobjective genetic algorithm: NSGA-II. *Evolutionary Computation, IEEE Transactions on* 2002; 6(2): 182–197. DOI:10.1109/4235.996017.
19. CES materials selector edupack. http://www.grantadesign.com /education/edupack.
20. Willmott A. *Dynamics of Regenerative Heat Tranfer*. Taylor & Francis, 2002.
21. Wakao N, Kaguei S and Funazkri T. Effect of fluid dispersion coefficients on particle-to-fluid heat transfer coefficents in packed beds: correlation of Nusselt numbers. *Chem Eng Sci* 1979; 34: 325–336.
22. Holdich RG. *Fundamentals of Particle Technology*. Midland Information Technology and Publishing, 2002.
23. Holman JP. *Heat Transfer*. 8/bk only edition ed. New York: Mcgraw-Hill College, 1997. ISBN 978-0-07-029722-7.

Appendix A: Numerical integration

The numerical scheme used to generate the results presented in this paper is based on that presented in Refs.[14;17] with some minor modifications in order to include heat leakage and axial conduction. Similar integration schemes may also be found in[20].

The thermal behaviour of the reservoirs is governed chiefly by the two energy equations (9 and 10), which are marched forward in space and time respectively along the paths indicated in Fig. 10. Except for the axial conduction term in the solid energy equation, all derivatives are coded implicitly. Thus,

$$\frac{T^n_{g,i} - T^n_{g,i-1}}{\Delta z} = \frac{\bar{T}^A_s - \bar{T}^A_g}{\ell} + F \tag{18}$$

$$\frac{T^n_{s,i} - T^{n-1}_{s,i}}{\Delta t} = \alpha \frac{T^{n-1}_{s,i+1} - 2T^{n-1}_{s,i} + T^{n-1}_{s,i-1}}{(\Delta z)^2} + \frac{\bar{T}^B_g - \bar{T}^B_s}{\tau_x} + + \frac{T_0 - \bar{T}^B_s}{\tau_l} \tag{19}$$

where quantities superscripted with A are averages between $(i-1, n)$ and (i, n), and those with B between $(i, n-1)$ and (i, n). F in Eq.(18) accounts for the unsteady gas accumulation term in Eq.(6) and is given by

$$F = \frac{\epsilon}{G c_{pg}} \left(\frac{\partial p}{\partial t} - \rho_g c_{pg} \frac{\partial T_g}{\partial t} \right) \tag{20}$$

Since this term is always small, it may be evaluated with sufficient accuracy at the upstream location, $(i-1)$. (It makes very little difference to the computed temperature

profiles, but is required to give the correct overall energy and exergy balances.)

Solution of equations (18) and (19) just requires inverting a 2×2 matrix at each node to obtain the two unknown temperatures at (i, n). Having obtained these temperatures, equations (8) and (4) are integrated with one-sided differences to obtain the pressure drop and the new mass flow rate per unit area, G, which varies slightly through the reservoir due to the changing gas density. Note that correlations are required for the Stanton number and friction coefficient. These have been taken from Refs.[21] and[22] respectively and take the form,

$$\begin{aligned} \mathrm{St} &= 2.0\mathrm{Pr}^{-1}{\mathrm{Re_p}}^{-1} + 1.10\mathrm{Pr}^{-2/3}{\mathrm{Re_p}}^{-2/5} \\ C_f &= 10{\mathrm{Re_m}}^{-1} + 0.8{\mathrm{Re_m}}^{-0.1} \end{aligned}$$

where $\mathrm{Re_p} = Gd_p/\mu_g$ and $\mathrm{Re_m} = G/(\{1-\epsilon\}S_v\mu_g$ are the particle and modified Reynolds numbers respectively. The effective conductivity of the bed k_{eff} has been set at $0.5\ \mathrm{Wm^{-1}K^{-1}}$ based on simple experiments on a representative sample of packing material (not described here due to space constraints).

The above-described scheme has been validated against the 'single-blow' analytical solution, first presented by Anzelius[8]. Details of the validation are presented in Ref.[17] where it is seen that the numerical and analytical solutions become indistinguishable for sufficiently small Δt and Δz. In practice, in order to obtain converged estimates for thermal loss (i.e., entropy generation rates), $\Delta z/\ell,\ \Delta t/\tau_x \lesssim 1/2$ is sufficient. (Due to the explicit coding of the diffusion term in Eq.(19), there is an additional stability constraint that $\alpha\Delta t/(\Delta z)^2 < 1/2$, but this only becomes relevant for very small particles.) As an example of CPU usage, a 5 m $\times$ 5 m $(L \times D)$ reservoir containing 8 mm diameter particles required 786 grid points, and required 2.6 seconds to compute 10 complete charge-discharge cycles on a standard desktop computer.

Appendix B: Insulation calculations

Determining the required thickness of insulation is based on three factors, namely (i) the fractional energy loss per day, (ii) the permissible non-uniformity in radial temperature distributions and (iii) the maximum allowable outside metal temperature. The first of these is readily estimated from a simple lumped-capacity heat transfer model, which may be expressed in the form

$$\frac{dE_s}{dt} = -U_\ell A_\ell (T_s - T_0) = -\frac{U_\ell A_\ell}{M_s \bar{c}_s} E_s = -\frac{E_s}{\tau_\ell} \qquad (21)$$

where A_ℓ is the surface area at the packing-insulation interface, and $\tau_\ell = M_s\bar{c}_s/U_\ell A_\ell$ is a heat-leakage time constant. Setting τ_ℓ to, say, 100 days corresponds to an *internal* energy loss rate of approximately 1% per day. (The fractional available energy loss will be somewhat higher, depending on T_s.) Thermal resistances are assumed to be dominated by the insulation, giving $U_\ell = k_i/t_i$ for ends and $k_i/\{R\ln(1+t_i/R)\}$ for sidewalls, t_i being the insulation thickness.

The lumped-capacity model results in a slight over-estimation of heat losses, due to the drop in packing temperature at its outer edge. However, since k_{eff}/k_i, is only of the order of 10:1, it is difficult to achieve sufficiently low Biot numbers in large reservoirs for the lumped-capacity model to be valid without excessive thicknesses of insulation. In such cases, radial non-uniformity is likely to be of greater concern than the level of heat leakage. Radial temperature variations in the packing are given by the standard solution to the unsteady cylindrically symmetric conduction problem (see for example Ref.[23]). Temperature profiles are shown in dimensionless form in Fig. 11 (a) for various Biot numbers, $\mathrm{B}i = U_\ell R/k_{\mathrm{eff}}$, and at times when the energy loss (i.e., average temperature drop) is 1% and 2%. As expected, uniform profiles are only obtained at very low Bi (~ 0.01), whereas in the current application Bi is typically > 0.5. Since it is not possible to fully assess the impact of radial variations on reservoir performance without recourse to two-dimensional calculations, the approach adopted here is to limit the outer edge temperature drop, $\Delta\theta_e$. This quantity is shown in Fig. 11 (b) as a function of the percentage energy loss for different Bi. As an example, if the reservoir is designed to have a 1% energy drop per day then limiting $\Delta\theta_e$ to 10% (in one day) requires that $Bi < 1.5$ (point A in the figure). Using material properties for magnetite and an insulation with $k_i = 0.05\mathrm{Wm^{-1}K^{-1}}$, this limits the packing diameter to 4.6m, and the corresponding insulation thickness (assuming $k_i = 0.05$) would be 16 cm. After two days, the energy loss would be $\sim 2\%$ and the outer-edge temperature would have dropped by 13% (point B).

Neglecting the surface heat transfer resistances in computing U_ℓ provides a conservative (i.e., over-) estimate for heat loss, but it is nonetheless necessary to consider the outside surface resistance in order to ensure that metal temperatures do not rise excessively. External heat transfer coefficients are estimated from the free-conctive correlation for a vertical plate, $\mathrm{N}u_L = (\mathrm{G}rPr)^{0.25}$, with L taken as R (corresponding to a half-charged reservoir). [3] On this basis it is seldom found that the external temperature rises by more than $40\ ^{\circ}\mathrm{C}$ above ambient; should it do so the insulation thickness is increased accordingly.

Appendix C: Approximate loss analysis

The optimum particle size required to minimise losses may be estimated on the basis of approximate expressions for entropy generation rates. This optimum is governed solely by the balance between thermal and pressure losses, but the conductive loss is also considered here for completeness.

Thermal loss. The expression for entropy generation due to gas-particle heat exchange (eq. 12) may be simplified by incorporating the gas energy equation (eq. 9) to give

$$\frac{\dot{S}_t}{\dot{m}c_{pg}} = \int_0^H \frac{\ell}{T_s T_g}\left(\frac{\partial T_g}{\partial z}\right)^2 dz \approx \left[f_t \frac{\Delta T^2}{T_c T_d}\right]\frac{\ell}{\lambda_t} \qquad (22)$$

The right hand approximation is obtained by noting that temperature gradients scale as $\Delta T/\lambda_t$, where λ_t is the length of the thermal front. The factor f_t (which is a weak function of T_c and T_d) is included to account for the shape of the front but, on the basis of estimates for a linear front, a value of unity is sufficient for the present approximations.

Pressure loss. Entropy generation due to the frictional pressure drop is approximated by noting that $\Delta p/p$ is usually small. Combining the expressions for pressure drop (eq. 8) and the associated entropy generation rate (eq. 13) with the definition of ℓ gives

$$\frac{\dot{S}_p}{\dot{m}c_{pg}} \approx \frac{(\gamma-1)\Delta p}{\gamma p} = \left[\frac{(\gamma-1)G^2 R\bar{T}_g}{2\gamma p^2 \epsilon^3}\frac{C_f}{\mathrm{St}}\right]\frac{\lambda_p}{\ell} \quad (23)$$

where λ_p is the length of packed bed through which the gas flows, and the use of an average temperature $\bar{T}_g$ accounts for the variation in gas density (and hence velocity) within the reservoir.

Conductive loss. As with the thermal loss, the entropy generation due to conduction along the bed depends on the steepness of the thermal front and so $\dot{S}_c$ and $\dot{S}_t$ are closely linked. This may be shown by comparing the above approximation for $\dot{S}_t$ (eq. 22) with Eq.(14). To a good approximation, this implies that

$$\frac{\dot{S}_c}{\dot{S}_t} \approx \frac{k_{\mathrm{eff}}}{Gc_{pg}\ell} = \frac{\ell_c}{\ell} \quad (24)$$

where $\ell_c = k_{\mathrm{eff}}/Gc_{pg}$ is a conductive length scale. This ratio between the conductive and thermal losses may also be derived by considering the two effective diffusivities described in the text following Eq.(11).

Minimum loss. Combining the above expressions, the total entropy generation rate due to irreversibility may be expressed in the form

$$\frac{\dot{S}_{\mathrm{irr}}}{\dot{m}c_{pg}} \approx K_t\frac{\ell}{\lambda_t} + K_p\frac{\lambda_p}{\ell} + K_t\frac{\ell_c}{\lambda_t} \quad (25)$$

where K_t and K_p are defined by the terms in square brackets on the right of equations (22) and (23) respectively. Differentiating with respect to ℓ and setting to zero yields

$$\ell^* \approx \sqrt{\lambda_t\lambda_p\frac{K_p}{K_t}} \quad (26)$$

$$\frac{\dot{S}^*_{\mathrm{irr}}}{\dot{m}c_{pg}} \approx 2\sqrt{K_tK_p\frac{\lambda_p}{\lambda_t}} + K_t\frac{\ell_c}{\lambda_t} \quad (27)$$

where the asterisk denotes the minimum loss condition. Values for λ_p and λ_t are required to proceed further and these depend on the use of layers or otherwise and the time history of charge and discharge. Only cyclic operation will be considered here.

Simple reservoirs. In this case the flow passes through the whole of the packed bed and so λ_p is always equal to H. By contrast, the thermal front length depends on the dimensionless cycle period Π as discussed in the cyclic operation section. With reference to Fig. 12, an approximation for λ_t may be obtained by equating the charge time t_c to the time taken for the front to travel a distance $H-\lambda_t$. In the hypothetical case of constant c_s, this gives $\lambda_t = (1-\Pi)H$. For variable c_s, λ_t may be taken as the average between λ_{t1} and λ_{t2} (see Fig. 12 (b)) leading to the same result. Substituting into Eqs. (26, 27) gives,

$$\frac{\dot{S}^*_{\mathrm{irr}}}{\dot{m}c_{pg}} = 2\sqrt{\frac{K_pK_t}{1-\Pi}} + \frac{K_t\ell_c}{(1-\Pi)H} \quad (28)$$

$$\text{at} \quad \ell^* = H\sqrt{\frac{K_p}{K_t}(1-\Pi)}$$

Since Π is approximately equal to the utilisation of the reservoir, Eq.(28) demonstrates the trade-off between high utilisation (and hence high energy density) and high efficiency.

Segmented reservoirs. The length of the flow path λ_p in this case depends on the number of layers and how they are controlled. In order to estimate the maximum achievable loss reduction, an ideal 'infinite-layer' scenario is considered in which the active layers track precisely the width of the thermal front, giving $\lambda_p = \lambda_t$. Assuming that λ_t is unaffected by the use of layers (which requires $\theta_l \approx 0$ and $\theta_h \approx 1$), Eqs. (26, 27) become

$$\frac{\dot{S}^*_{\mathrm{irr}}}{\dot{m}c_{pg}} = 2\sqrt{K_pK_t} + \frac{K_t\ell_c}{(1-\Pi)H} \quad (29)$$

$$\text{at} \quad \ell^* = (1-\Pi)H\sqrt{\frac{K_p}{K_t}}$$

The first term in the expression for $\dot{S}_{\mathrm{irr}}$ (which is the sum of pressure and thermal losses, and usually dominates) is now independent of Π. In theory this should allow optimisation at close to full utilisation by using very small particles and many layers. In practice, growth of the thermal front due to the temperature dependence of c_s limits the maximum value of Π, and the conductive term in any case becomes more significant at high utilisation.

Values of K_t, K_p and l_c for the three reservoirs are given in Table 3 together with corresponding optimum particle sizes and minimum losses ζ^* expressed as percentage losses in availability. The agreement with numerical results for d^*_p and ζ^* is very reasonable given the approximations involved, although losses tend to be under predicted for the segmented reservoirs for the reasons discussed in the section on optimum particle size. Aside from speed of computation, the foregoing approximate method has the benefit of revealing functional dependence on the design parameters. Thus, for example, the the minimum loss (ignoring the conductive component) scales as G which in turn scales as $(H/D)^{2/3}$ at fixed storage volume.

FIGURES

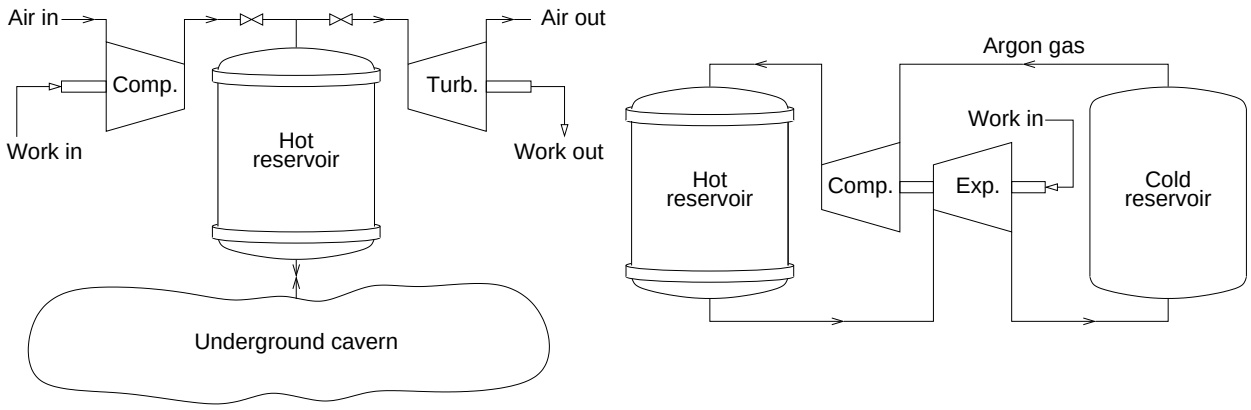

(a) Simplified Adiabatic CAES (b) PTES shown during charge

Figure 1. Examples of electrical energy storage systems that make use of packed-bed thermal reservoirs

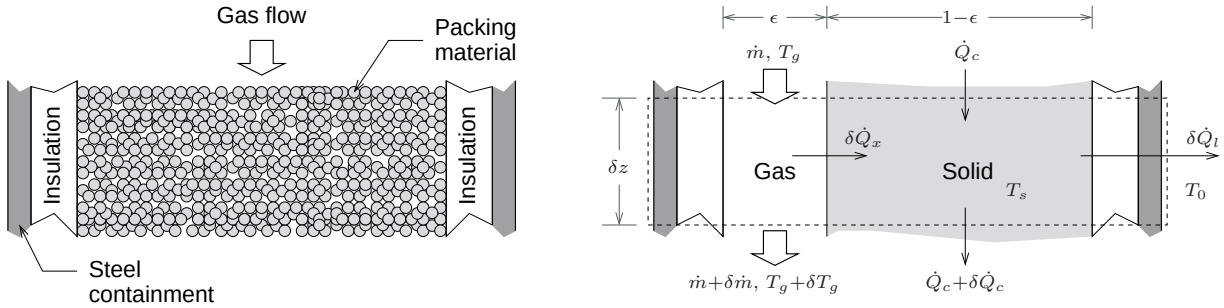

(a) Basic structure (b) Equivalent control volume

Figure 2. Basic construction of a (hot) packed-bed reservoir and the equivalent control volume (during charge). $\dot{Q}_c$, $\dot{Q}_l$ and $\dot{Q}_x$ are heat transfer rates due to conduction along the bed, wall leakage and gas-solid heat exchange respectively.

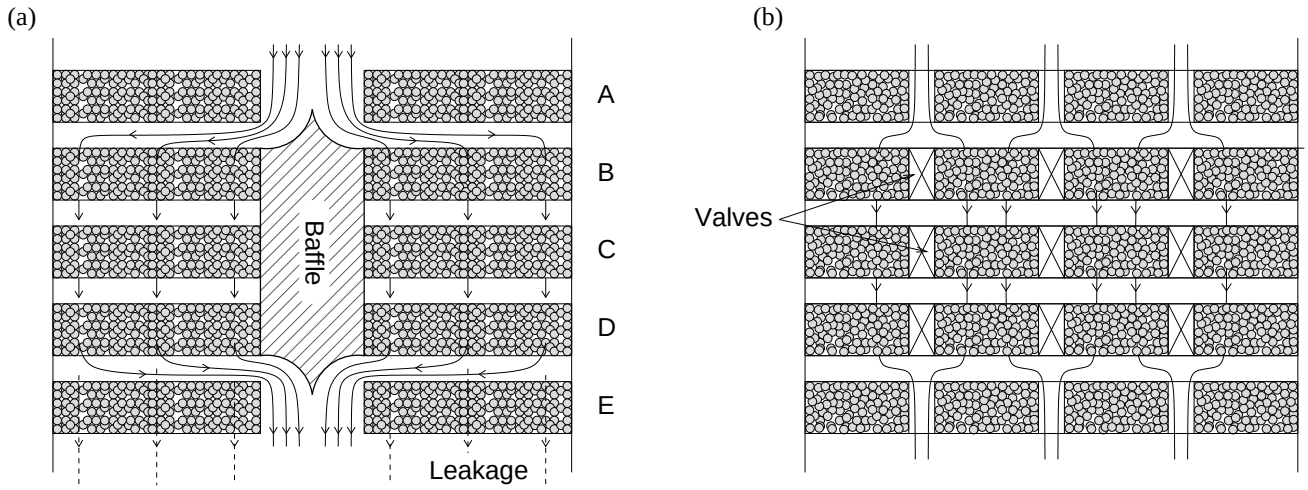

Figure 3. Schematic of possible layer-control arrangements for segmented reservoirs, based on Refs.[7;16]. **(a)** A fixed number of layers are kept active by the baffle arrangement. **(b)** Independent valving on each layer allows greater flexibility.

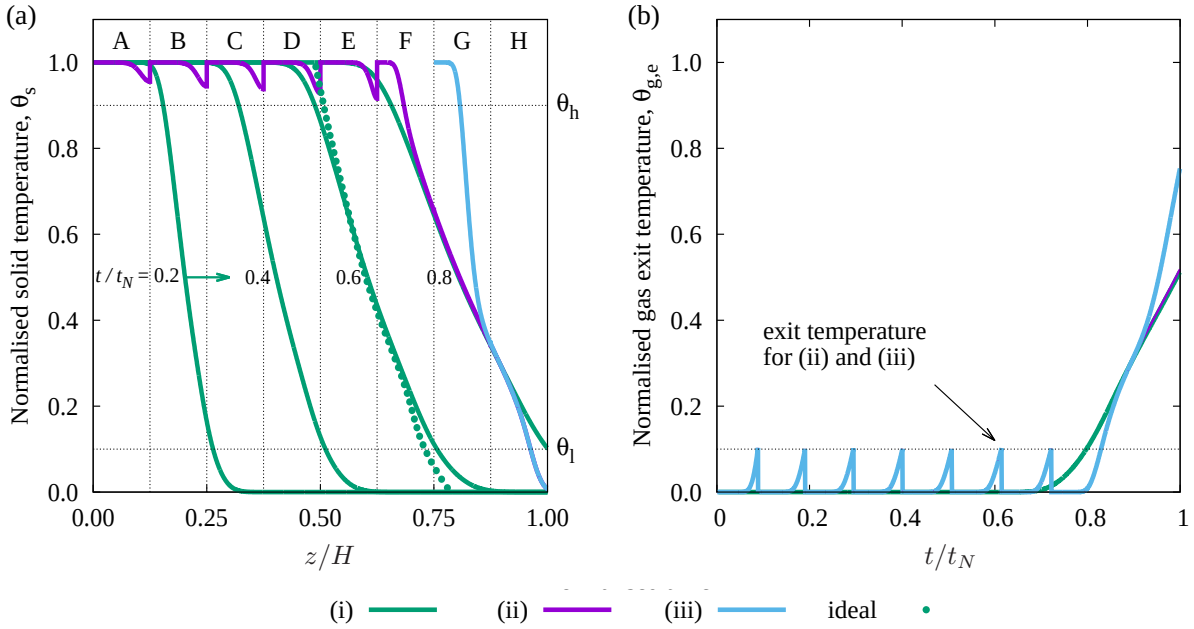

Figure 4. Single charge operation of R1 (hot reservoir for 2MW PTES with a nominal 8 hours storage): **(a)** solid temperature profiles; **(b)** gas exit temperatures. Case (i) is unsegmented, cases (ii) and (iii) have 8 segments but different control methods. The particle diameter is $d_p = 4$ mm.

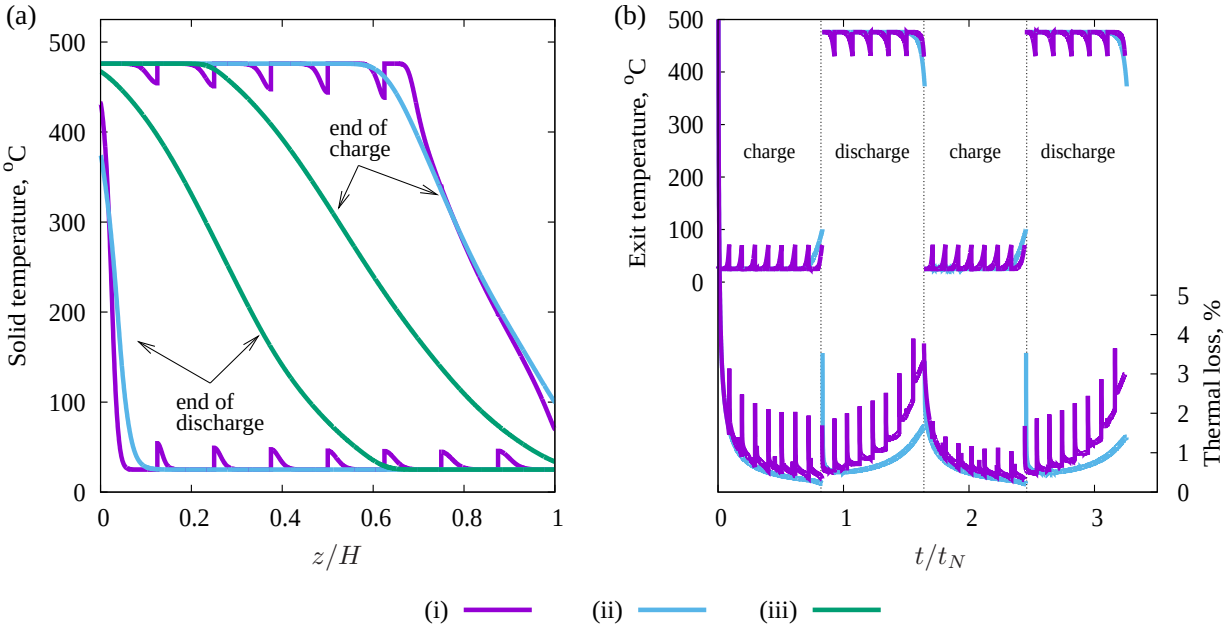

Figure 5. Cyclic operation of R1 (hot resevoir for 2MW PTES with a nominal 8 hours of storage) with $d_p = 4$ mm: **(a)** temperature profiles and **(b)** exit temperatures and thermal losses. Cases: (i) 8 layers, $\Pi \approx 0.8$; (ii) simple reservoir, $\Pi \approx 0.8$; (iii) simple reservoir, $\Pi \approx 0.3$

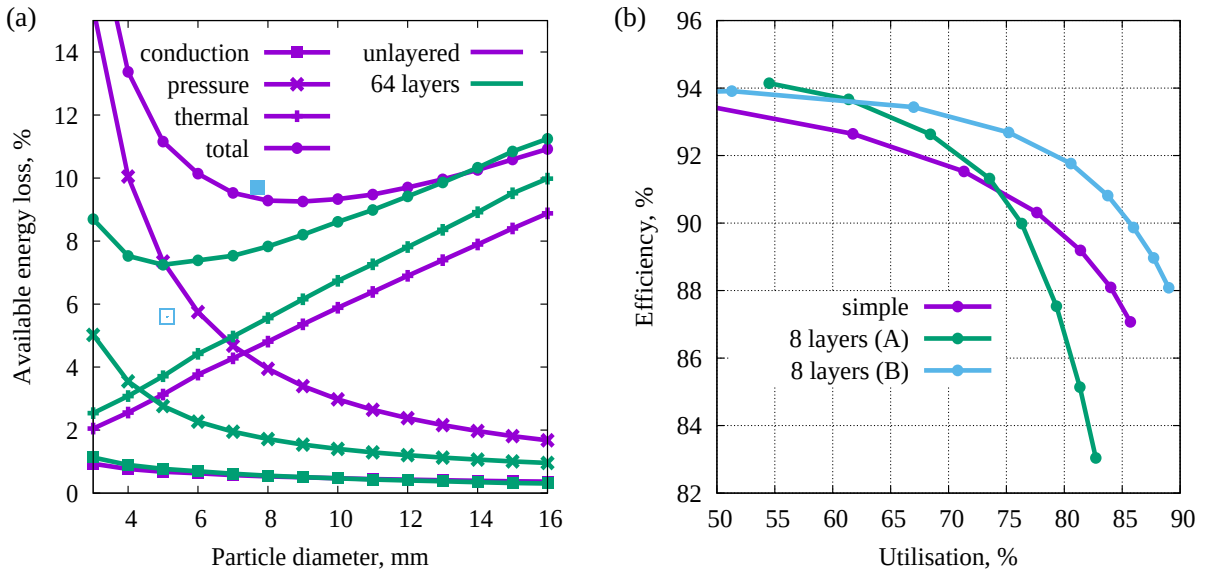

Figure 6. **(a)** Loss vs. particle size for simple and 64-layered R2 (cold reservoir for 2 MW PTES) at $\Pi = 0.7$; Points ■ and ⊡ are the optima based on Appendix C. **(b)** Efficiency vs. utilisation for simple and 8-layered R2 optimised for $\Pi = 0.7$ (see text for A and B).

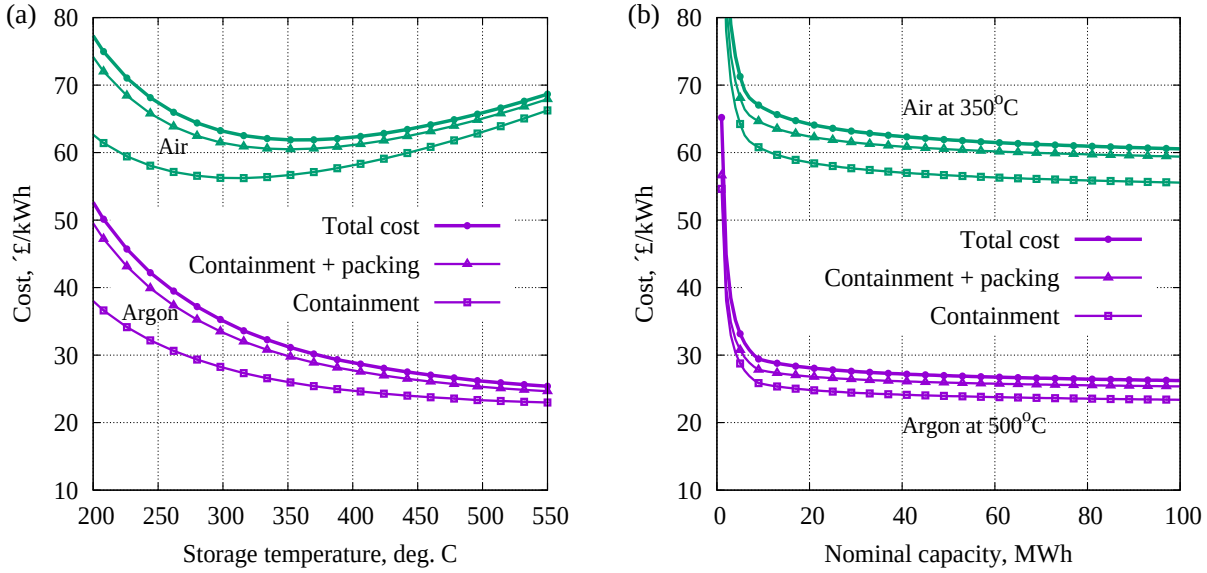

Figure 7. Estimated costs per kWh capacity vs. **(a)** storage temperature for 50 MWh capacity; **(b)** storage capacity at specified temperatures. Pressures are calculated from isentropic relations. Total cost = containment + packing + insulation.

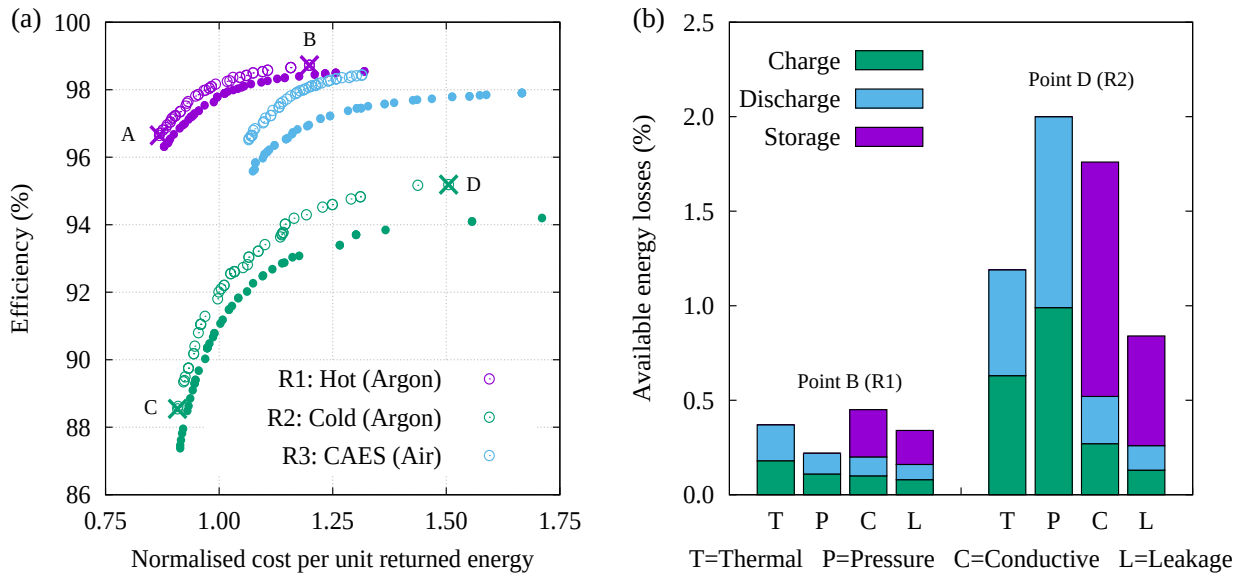

Figure 8. **(a)** Pareto fronts showing trade-off between efficiency and costs. Solid and open symbols are for simple and segmented reservoirs respectively. **(b)** Distribution of losses for selected (high efficiency) points B and D.

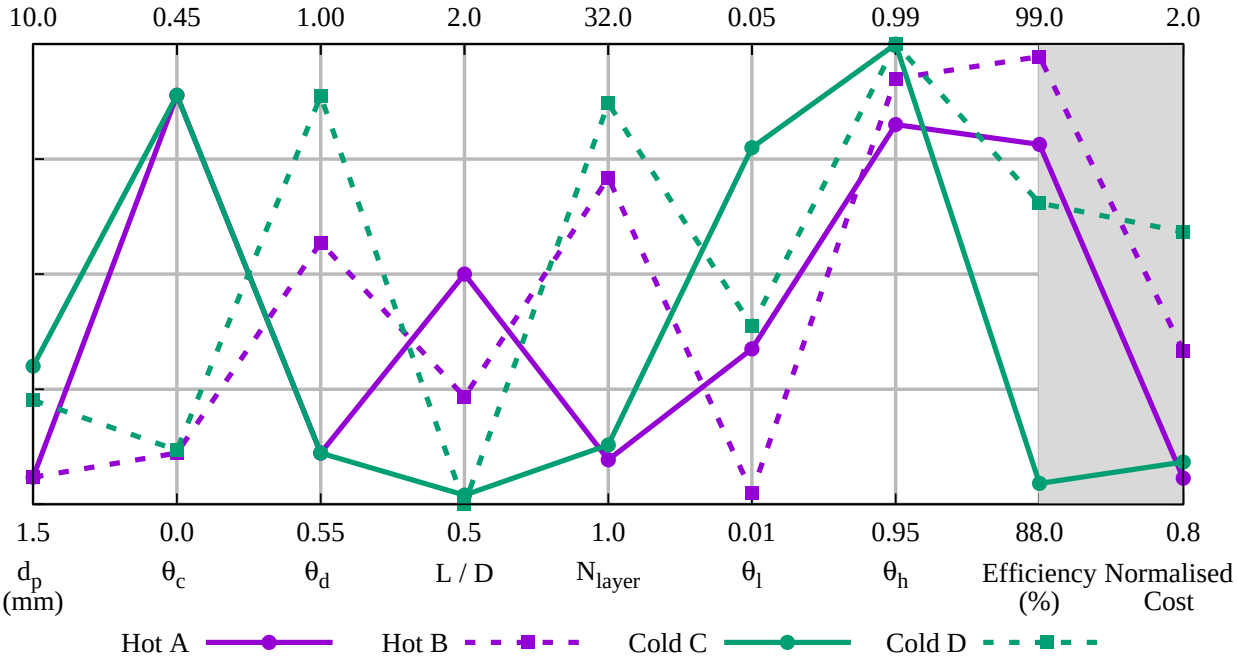

Figure 9. Parallax plot showing design parameters for points A and B (hot reservoir R1) and C and D (cold reservoir R2)

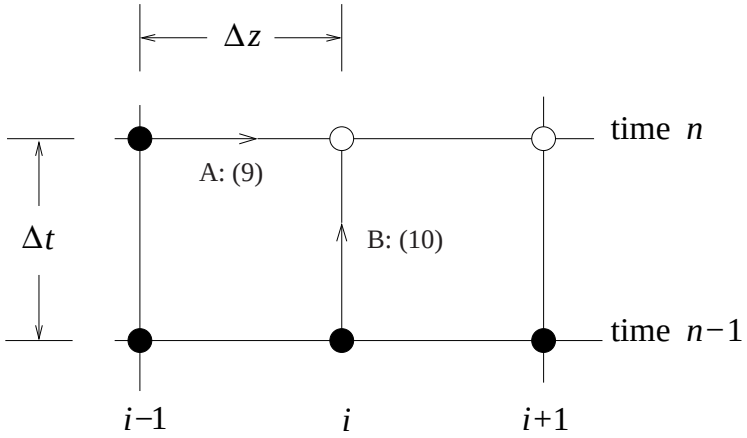

Figure 10. A section of the computational grid: properties are known at nodes marked • and unknown at those marked ○. The two energy equations are integrated along the paths A and B shown to obtain T_g and T_s at node (i, n).

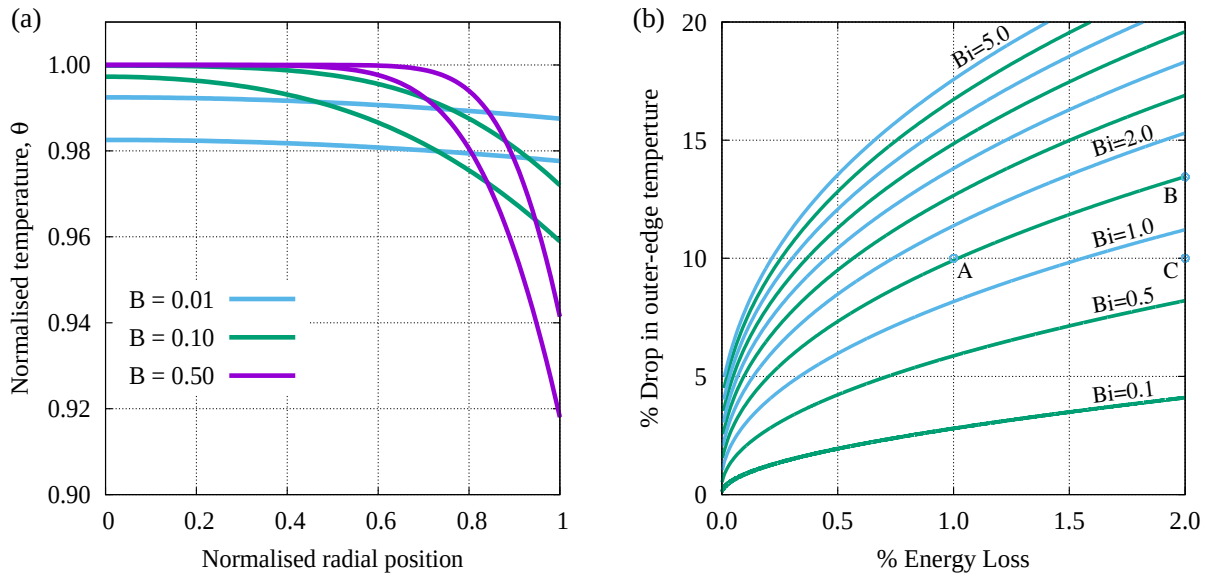

Figure 11. Unsteady heat conduction through the packing material: **(a)** radial profiles, $\theta = (T_s(r) - T_0)/(T_s(0) - T_0)$ vs. r/R shown at 1 % and 2 % energy drop; **(b)** drop in $\theta(1)$ as a function of energy loss for different Biot numbers.

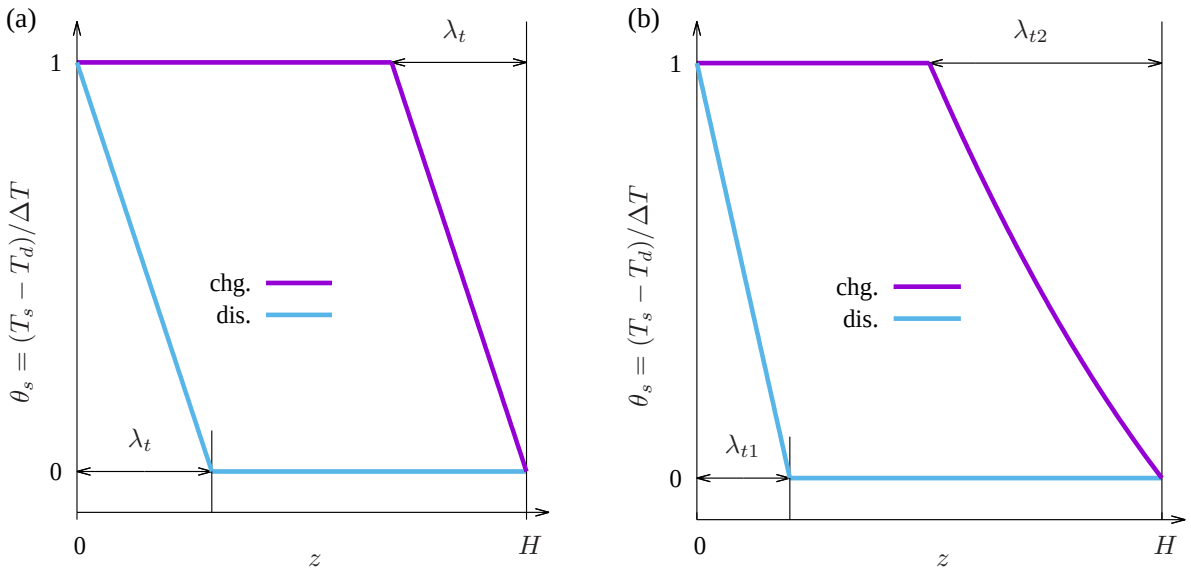

Figure 12. Schematic of thermal fronts at the end of charge and discharge for (a) constant c_s and (b) temperature-dependent c_s. Charge and discharge periods are assumed to end when the leading edge of the front reaches the exit.

TABLES

RESERVOIR:	**R1**	**R2**	**R3**
Application	PTES (hot)	PTES (cold)	CAES
Working fluid	Argon	Argon	Air
Operating pressure, p	10.5 bar	1.05 bar	15.0 bar
Charge temperature:, T_c	476 °C	-154 °C	412 °C
Discharge temperature, T_d	25 °C	25 °C	25 °C
Reservoir diameter, D	4.62 m	5.45 m	7.70 m
Reservoir height, H	4.62 m	5.45 m	23.1 m
Mass flow rate, $\dot{m}$	13.7 kg/s	13.7 kg/s	95.1 kg/s

Table 1. Geometry and operating conditions of reservoirs. The storage material is $\mathrm{Fe_3O_4}$ with $\epsilon = 0.4$ in all cases.

	Geometric parameters			Operational parameters			
	L/D	d_p (mm)	N_{seg}	θ_c	θ_d	θ_l	θ_h
Nominal	1.0	20.0	1	0.25	0.75	(-)	(-)
Minimum	0.5	1.50	1	0.05	0.50	0.01	0.95
Maximum	2.0	50.0	32	0.50	0.95	0.05	0.99

Table 2. Parameters varied during optimisation. θ_l and θ_h are normalised exit temperatures from interior segments (see Fig. 4); θ_c and θ_d are corresponding values in the last segment during charge and discharge respectively.

					Simple		**Segmented**	
		K_t –	K_p $\times 10^{-6}$	l_c (mm)	d_p^* (mm)	ζ^* (%)	d_p^* (mm)	ζ^* (%)
R1	Approximate theory	0.92	0.76	1.18	**2.7**	**1.28**	**1.8**	**0.82**
	Numerical results	–	–	–	**3.0**	**1.21**	**2.0**	**0.92**
R2	Approximate theory	0.90	11.0	1.66	**7.7**	**9.7**	**5.1**	**5.6**
	Numerical results	–	–	–	**8.1**	**9.3**	**5.1**	**7.2**
R3	Approximate theory	0.74	2.60	0.47	**7.9**	**2.6**	**4.4**	**1.2**
	Numerical results	–	–	–	**8.9**	**2.3**	**4.1**	**1.3**

Table 3. Comparison of estimated and computed optimum particle diameters and corresponding losses. R1 and R2 (hot and cold reservoirs for PTES) are calculated with $\Pi = 0.7$ and R3 (CAES) with $\Pi = 0.8$